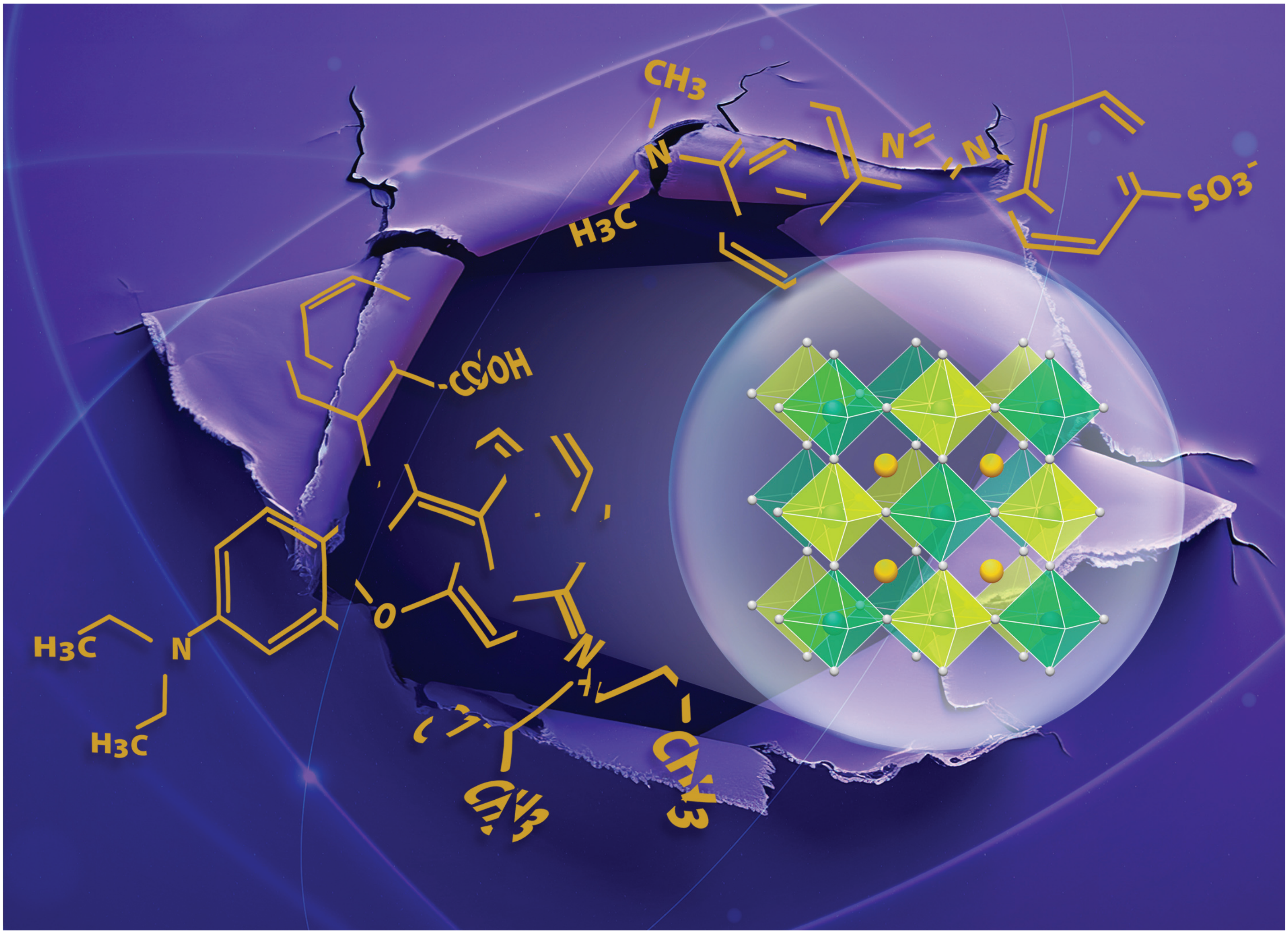

Showcasing research from Professor Nora S. Portillo-Vélez and Professor Hugo A. Lara-García laboratories, Departamento de Química (UAMI) and Instituto de Física (IFUNAM), Universidad Autónoma Metropolitana and Universidad Nacional Autónoma de México, CDMX, Mexico.

Facile ultrasound-assisted synthesis of $Cs_2AgBiBr_6$ nanocrystals for enhanced visible-light photocatalysis

We report a new, simple, low-cost, and environmentally friendly ultrasound-assisted method for synthesising 6 nm $Cs_2AgBiBr_6$ nanocrystals at room temperature and under ambient air. The nanocrystals exhibit high phase purity, structural stability, and improved photocatalytic performance under visible light, retaining their activity over repeated cycles. This scalable approach provides a practical and sustainable route for developing efficient lead-free halide perovskites for environmental applications.

Image reproduced by permission of Instituto de Física, UNAM from *Dalton Trans.*, 2025, **54**, 17418.

As featured in:

See Nora S. Portillo-Vélez, Hugo A. Lara-García *et al.*, *Dalton Trans.*, 2025, **54**, 17418.

ROYAL SOCIETY OF **CHEMISTRY**

rsc.li/dalton

Dalton
Transactions

COMMUNICATION

View Article Online
View Journal | View Issue

Cite this: *Dalton Trans.*, 2025, **54**, 17418

Received 15th June 2025,
Accepted 20th August 2025

DOI: 10.1039/d5dt01406a

rsc.li/dalton

Facile ultrasound-assisted synthesis of $Cs_2AgBiBr_6$ nanocrystals for enhanced visible-light photocatalysis

Emmanuel Godínez,[a] Jennyfer Moreno,[a] Sergio Chang,[a] Victor Hugo Guzman,[a] Yesenia A. García-Jomaso,[a] Herlinda Montiel,[b] Nora S. Portillo-Vélez *[c] and Hugo A. Lara-García *[a]

We report a novel, simple, and environmentally friendly ultrasound-assisted method for the synthesis of $Cs_2AgBiBr_6$ nanocrystals. The synthesis is performed entirely at room temperature and under ambient air, without the need for inert atmospheres. Transmission electron microscopy (TEM) confirms an average particle size of approximately 6 nm, while X-ray diffraction (XRD) and Raman spectroscopy verify the high phase purity and structural stability of the nanocrystals. These nanocrystals exhibit enhanced photocatalytic activity under visible light, achieving complete degradation of rhodamine B in 60 minutes. This improved performance, compared to bulk $Cs_2AgBiBr_6$, is attributed to the increased surface area and more efficient charge carrier separation at the nanoscale. The nanocrystals also show good stability over multiple cycles and can degrade methyl orange, highlighting their versatility. Electron paramagnetic resonance (EPR) measurements confirm the formation of superoxide radicals ($^{\bullet}O_2^-$) as the primary active species, supporting a surface-driven photocatalytic mechanism. Unlike conventional hot-injection methods, this approach is low-cost, scalable, and sustainable. It offers a practical route for the development of lead-free halide perovskite materials for environmental and energy-related applications.

In recent years, halide perovskites have garnered significant attention due to their outstanding optoelectronic properties, positioning them as promising candidates for applications such as in solar cells, light-emitting diodes, and particularly photocatalysis.[1–3] While lead halide perovskites exhibit excellent optoelectronic properties, their intrinsic toxicity and poor stability under ambient conditions represent considerable challenges for commercial deployment. Consequently, substantial efforts have been made towards the development of lead-free perovskites that preserve the desirable properties of their lead-based counterparts while addressing concerns related to toxicity and stability.[4–6]

Among the most promising candidates are the double halide perovskites, particularly bismuth-based[7] compounds such as $Cs_2AgBiBr_6$.[8] Initial studies centred on their application in photovoltaics; however, the moderate charge carrier mobility and indirect bandgap limited their performance in solar cells.[9,10] Interest subsequently shifted towards photocatalysis, where such limitations are less critical, and surface-mediated processes dominate.[11–15]

$Cs_2AgBiBr_6$ exhibits several characteristics that make it a promising candidate for photocatalytic applications. Its moderate indirect bandgap (approximately 1.9–2.5 eV) allows efficient absorption of visible light, thereby enabling the utilisation of a broad portion of the solar spectrum. The material also possesses a relatively high dielectric constant, which facilitates charge separation by lowering the exciton binding energy.[16–19] Furthermore, its excellent structural and chemical stability under moisture, thermal, and light exposure conditions ensures long-term durability during photocatalytic processes.[20–24] When prepared as nanocrystals, $Cs_2AgBiBr_6$ provides an increased surface-to-volume ratio and enhanced surface reactivity, both of which are critical for promoting efficient interfacial charge transfer.

Since the first report in 2018 by Zhou *et al.*, who synthesised cubic $Cs_2AgBiBr_6$ nanocrystals *via* a hot injection method for CO_2 photoreduction, various studies have explored its application in dye degradation.[19] Zhang *et al.* demonstrated the photocatalytic degradation of dyes in ethanol, confirming the stability of the perovskite after the reaction.[25] More recently, $Cs_2AgBiBr_6$ synthesised *via* mechanosynthesis achieved complete degradation of rhodamine B in just 60 minutes, underscoring the importance of synthesis conditions in optimizing photocatalytic performance.[26]

Further studies have demonstrated that the particle size of $Cs_2AgBiBr_6$ has a significant impact on its photocatalytic per-

---

[a] *Instituto de Física, Universidad Nacional Autónoma de México, Apartado Postal 20-364, Ciudad de México 01000, Mexico. E-mail: hugo.lara@fisica.unam.mx*
[b] *Instituto de Ciencias Aplicadas y Tecnología, Universidad Nacional Autónoma de México, Circuito Exterior, Ciudad Universitaria Coyoacan, 04510 Mexico City, Mexico*
[c] *Departamento de Química, Área de Catálisis, Universidad Autónoma Metropolitana-Iztapalapa, Av. San Rafael Atlixco No. 189, Iztapalapa, Ciudad de México 09340, Mexico. E-mail: noraportillo@xanum.uam.mx*

formance. For instance, quantum dots obtained *via* a modified hot-injection method have shown remarkable efficiency in the degradation of dyes and antibiotics.[27] Nevertheless, this technique typically requires high temperatures (>100 °C) and inert atmospheres, which limits its practical scalability. In this work, we report a novel ultrasound-assisted synthesis of $Cs_2AgBiBr_6$ nanocrystals conducted under ambient conditions. The resulting nanocrystals, with an average particle size of approximately 6 nm, exhibit enhanced photocatalytic activity under visible light, achieving complete degradation of rhodamine B within 60 minutes, significantly outperforming their microcrystalline counterparts.

The $Cs_2AgBiBr_6$ nanocrystals were synthesised *via* an ultrasound-assisted method at room temperature under ambient conditions, without the need for an inert atmosphere (Fig. S1). Oleic acid (OA), 1-octadecene (ODE), and oleylamine (OAm) were employed as surfactants. In a typical synthesis, 0.194 g of Cs_2CO_3, 0.100 g of $AgNO_3$, and 0.268 g of $BiBr_3$ were placed in a 20 mL vial, followed by the addition of 530 μL of HBr, 1 mL of OA, 1 mL of OAm, and 10 mL of ODE. The mixture was subjected to ultrasonic treatment using a UH-650 W ultrasonic homogeniser at 40% power with a pulse cycle of 2 s on and 1 s off, carried out in an ice bath to prevent overheating.

The optimisation process was performed in three stages: (i) the amount of HBr was initially varied and subsequently fixed at 265 μL, after which the ligand concentrations were adjusted; (ii) all precursor masses and the HBr volume were then doubled to 530 μL while keeping the optimised ligand amounts constant, yielding nanocrystals with superior optical responses compared to the synthesis using half the precursor quantities; and (iii) the sonication time was varied, identifying an optimal time of 20 minutes. The synthesis progress was monitored by UV–Vis absorbance (Fig. S2), and the optimal parameters were selected when the characteristic absorption peak of $Cs_2AgBiBr_6$ nanocrystals was clearly defined, leading to the final conditions described above.

The crystal structure was analysed by X-ray diffraction and Raman spectroscopy. Fig. 1a shows the XRD pattern of the as-prepared perovskite compared with the simulated diffraction pattern. Only reflections corresponding to the $Cs_2AgBiBr_6$ phase are observed, with no secondary phases detected. To further confirm the phase purity, Raman spectra were collected at four different regions of the sample (labelled $Cs_2AgBiBr_6$-1 to -4 in Fig. 1b) to account for local variations, as the measurement is spatially confined by the focused laser. Fig. 1b presents the Raman spectra, showing four characteristic peaks at 60, 78, 138, and 177 cm^{-1}, corresponding to the $F_{2g}^{(1)}$, $F_{2g}^{(2)}$, E_g, and A_{1g} modes, respectively. The A_{1g} mode involves a symmetric breathing vibration of the six Br atoms around the central Ag atom. The E_g mode represents a similar motion, with three Br atoms moving toward and three moving away from the Ag atom. In the $F_{2g}^{(1)}$ mode, Cs atoms contribute to the vibrations alongside Br, and in the $F_{2g}^{(2)}$ mode, all atoms participate.[28] The absence of additional peaks in the Raman spectra further supports the phase purity of the sample.

The morphology and particle size of the synthesized nanocrystals were investigated using TEM. Fig. 2a–c present TEM images at different magnifications, offering a global view of the nanoparticles obtained by the ultrasound-assisted method. The nanoparticles exhibit a polymorphic appearance with sizes below 10 nm, and an average diameter of 6 nm (see Fig. S3). These dimensions are comparable to those reported for $Cs_2AgBiBr_6$ synthesised *via* the hot injection method,[19,24,29] and smaller than those produced by the ligand-assisted reprecipitation (LARP) method[30] or the antisolvent approach. These results confirm that the ultrasound-assisted method is a successful and efficient strategy for synthesising $Cs_2AgBiBr_6$ nanoparticles under ambient conditions. In Fig. 2c, the interplanar distances of two representative nanocrystals are shown. The particle on the left exhibits a lattice spacing of 2.82 Å, corresponding to the (400) plane, while the one on the right displays a spacing of 3.28 Å, assigned to the (222) plane, both consistent with the cubic structure of $Cs_2AgBiBr_6$.

The optoelectronic properties of the $Cs_2AgBiBr_6$ nanocrystals were investigated using UV-Vis absorption spectroscopy and photoluminescence (PL). Fig. 3a displays the UV-Vis absorption spectrum of the nanocrystals dispersed in isopropanol. A distinct excitonic peak is observed around 440 nm, accompanied by a broad absorption tail extending towards

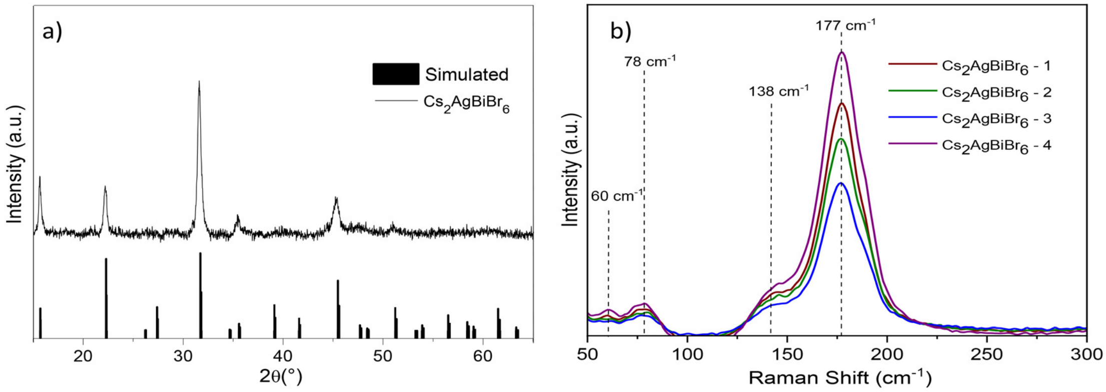

Fig. 1 (a) X-ray diffraction pattern and (b) Raman spectra of $Cs_2AgBiBr_6$ nanocrystals.

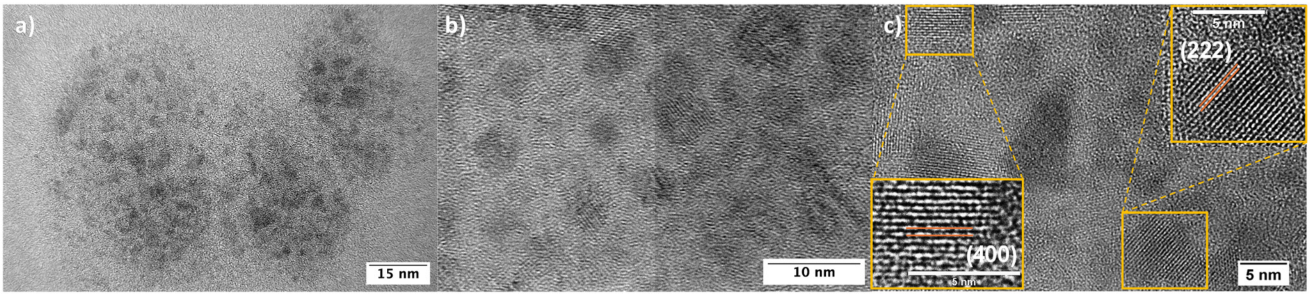

Fig. 2 (a–c) Transmission Electron Microscopy (TEM) images of $Cs_2AgBiBr_6$ nanocrystals at increasing magnifications, (c) shows lattice fringes of two particles: the left one has a spacing of 2.82 Å (400) and the right one, 3.28 Å (222).

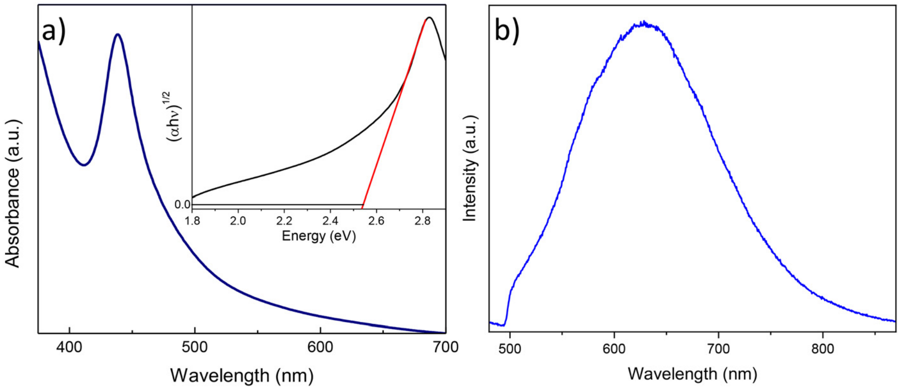

Fig. 3 (a) The UV-Vis absorption spectrum, Tauc plot (inset), and (b) photoluminescence (PL) spectrum of $Cs_2AgBiBr_6$ nanocrystals.

longer wavelengths. This spectral behaviour is characteristic of an indirect bandgap, which is consistent with the known electronic structure of $Cs_2AgBiBr_6$. The optical response observed here closely resembles that reported for $Cs_2AgBiBr_6$ nanocrystals synthesised by various other methods,[19,31–34] with the exception of a single study that reported a spectrum more typical of the bulk material.[35] Notably, no additional absorption features are detected in the 380–400 nm range, which suggests the absence of the $Cs_3Bi_2Br_9$ phase, one of the most common secondary phases in this family of double perovskites.[28] This finding indicates the high phase purity of the nanocrystals synthesised by our method. The bandgap was estimated to be 2.5 eV using the Tauc plot method, assuming an indirect allowed electronic transition. The Tauc plot was constructed by plotting $(\alpha h\nu)^{1/2}$ against photon energy, and the bandgap was determined by extrapolating the linear region to the energy axis (see the inset of Fig. 3a). The resulting value lies within the visible spectral range, which is an advantage for performing photocatalysis under visible light irradiation.

The photoluminescence (PL) spectrum of the $Cs_2AgBiBr_6$ nanocrystals, as shown in Fig. 3b, reveals a broad emission band centred around 630 nm, significantly red-shifted relative to the absorption edge. This emission is characteristic of the indirect bandgap nature of $Cs_2AgBiBr_6$ and is commonly attributed to radiative recombination involving self-trapped excitons or colour centers.[36,37] The relatively low intensity of the PL signal is consistent with the known behaviour of double perovskites with indirect transitions, where the momentum mismatch between the minimum conduction band and the valence band maximum reduces radiative recombination efficiency.

In order to compare the photocatalytic activity of the nanocrystals synthesised by the ultrasound-assisted method, single crystals of $Cs_2AgBiBr_6$ were grown *via* a solvothermal method. These crystals were then mechanically milled and sieved to obtain a fine powder. The resulting powder was characterised by X-ray diffraction (Fig. S4), scanning electron microscopy (SEM), UV-Vis diffuse reflectance spectroscopy, and photoluminescence (PL).

SEM images of the powders (Fig. S5) reveal that the particle size is in the micrometre range. For comparison purposes, N_2 adsorption–desorption measurements were performed. Fig. S6 clearly shows that nanocrystals exhibit a significantly higher N_2 uptake compared to microcrystals. Nevertheless, the BET surface areas for both samples remain low, in all cases below 1 m^2 g^{-1}, with the nanocrystals displaying a value approximately one order of magnitude higher than that of the microcrystals. In the case of nanocrystals, this limited surface area is attributed to the presence of residual organic ligands, such as oleic acid and oleylamine, remaining after the washing process. While these ligands are essential to preserve colloidal stability, they partially block the access of N_2 molecules to the surface. Complete ligand removal, on the other hand, would promote nanoparticle agglomeration, further reducing the accessible surface area.

The UV-Vis spectrum (Fig. S7) is characteristic of bulk $Cs_2AgBiBr_6$, exhibiting a distinct excitonic peak at 419 nm, as observed in the nanocrystal sample, followed by a broad absorption attributed to free charge carriers. The optical bandgap, calculated using the Tauc plot method and assuming an indirect allowed transition, was found to be 2.1 eV. The PL spectrum (Fig. S8) is centred at 641 nm, consistent with the redshift previously discussed for this material.

To evaluate the photocatalytic activity of the synthesised materials, the degradation of rhodamine B (RhB) in ethanol under visible light irradiation was used as a model reaction. Both the $Cs_2AgBiBr_6$ nanocrystals and the bulk powder were tested under identical conditions, using 20 mg of photocatalyst in 200 mL of a 10 ppm RhB solution in ethanol under visible light. Rhodamine B (RhB) was selected as a model probe due to its faster degradation rate compared to rhodamine 110, methyl red, and methyl orange.[25]

Fig. 4a shows the results of the photolysis and adsorption tests using the nanocrystals. After 90 minutes, photolysis alone caused negligible RhB degradation, while adsorption removed approximately 10% of the dye. These experiments confirm that subsequent degradation is driven by the photocatalyst rather than direct photodecomposition. Accordingly, all photocatalytic experiments were preceded by 30 minutes of dark stirring to reach adsorption–desorption equilibrium.

Fig. 4b shows the characteristic UV-Vis absorption peaks of RhB using the nanocrystals as a photocatalyst, with particular attention to the peak at 552 nm, which corresponds to the maximum absorbance of RhB in solution. With increasing irradiation time, the intensity of this peak gradually decreased, indicating progressive dye degradation, and it nearly vanished after the complete reaction, confirming almost total RhB removal under visible light with aeration.

Fig. 4c shows the comparison of the photocatalytic efficiency of nanocrystals and bulk-derived powder. Experiments were performed in triplicate, with error bars representing standard deviation. Nanocrystals achieved >95% RhB degradation within 60 minutes, whereas bulk powder degraded only ~75% after 60 minutes. This enhanced performance arises from the smaller nanocrystal size (<30 nm, below the typical diffusion length of photogenerated carriers),[38] which promotes efficient charge separation and minimizes bulk recombination. The larger bulk crystallites exhibit slower carrier diffusion, increasing recombination probability. Additionally, the higher surface-to-volume ratio of nanocrystals provides more active sites for photocatalysis.

Several studies have investigated the photocatalytic performance of pure $Cs_2AgBiBr_6$ under different conditions. While some report excellent degradation under UVC light (*e.g.*, 100% RhB removal in 75 minutes using 25 mg in water), such conditions are less practical due to the use of UV sources and the material's known instability in aqueous media.[26] In contrast, our system, operating under visible light with 20 mg of catalyst in 200 mL of ethanol, achieved 99% RhB degradation in 60 minutes, demonstrating high efficiency under milder and more scalable conditions. Other visible-light studies show lower performance; for instance, one report achieved only 45% degradation in 25 minutes using 40 mg of catalyst in just 50 mL of ethanol,[21] while another required 120 minutes to reach complete degradation.[25] A notable exception is a study that achieved 98% degradation in only 10 minutes using 20 mg of catalyst in 100 mL of ethanol, which outperforms our system.[35] However, that study used ultrasmall ~2 nm $Cs_2AgBiBr_6$ nanocrystals, synthesised *via* a hot-injection method that requires high temperatures, inert atmospheres, and stringent control over reaction conditions. In contrast, our nanocrystals (~6 nm) were obtained *via* a simpler, low-temperature route. Despite the larger size, our results remain highly competitive, highlighting not only the strong intrinsic photocatalytic activity of $Cs_2AgBiBr_6$ but also the practical advantages and scalability of our synthesis approach (Table 1).

Moreover, the degradation kinetics further underscore these differences. The nanocrystals display an exponential decay profile consistent with first-order reaction kinetics, reflecting efficient photocatalytic degradation driven by

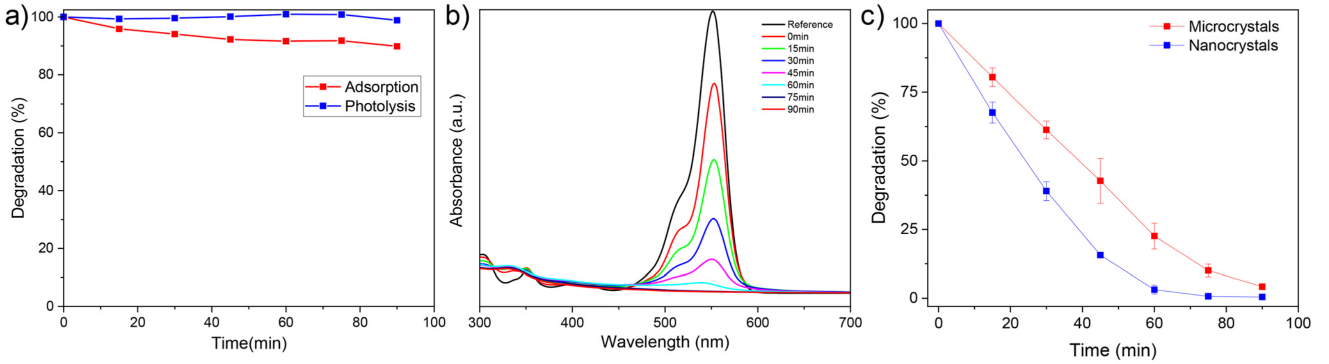

Fig. 4 (a) Photolysis and adsorption behaviour of rhodamine B; (b) UV–Vis absorption spectra of RhB as a function of irradiation time; and (c) comparative photocatalytic activity of $Cs_2AgBiBr_6$ nanocrystals and microcrystals; the experiments were performed in triplicate, and the error bars represent the standard deviation.

Table 1 Comparison of RhB dye degradation efficiencies using $Cs_2AgBiBr_6$-based photocatalysts

Sample	Dye	Light	Solvent	Amount of catalyst	Time	% dye removal	Ref.
$Cs_2AgBiBr_6$	RhB	UVC	Water (150 mL)	25 mg	75 min	100%	26
$Cs_2AgBiBr_6$	RhB	Visible	Ethanol (50 mL)	40 mg L^{-1}	25 min	45%	21
$Cs_2AgBiBr_6$	RhB	Visible	Ethanol (10 mL)	20 mg	120 min	100%	25
$Cs_2AgBiBr_6$	RhB	Visible	Ethanol (100 mL)	20 mg	10 min	98%	35
$Cs_2AgBiBr_6$	RhB	Visible	Ethanol (200 mL)	20 mg	60 min	99%	This work

surface-mediated processes. In contrast, the bulk powder exhibits a more linear degradation trend, indicative of a slower, diffusion-limited mechanism, likely due to a reduced number of accessible active sites and less effective interaction between the photocatalyst surface and RhB molecules.

To further quantify the degradation process, the kinetics were modelled using standard kinetic models. For the nanocrystals, the data fit well to a pseudo-first-order model, described by the equation $\ln(C/C_0) = -kt$. A linear fit of the experimental data (Fig. S9a) yielded a correlation coefficient of $R^2 = 0.96$ and a rate constant of $k = 0.0622\ \text{min}^{-1}$, indicating that the degradation rate is proportional to the concentration of RhB. This kinetic behaviour suggests efficient photogenerated charge carrier separation and transfer at the nanocrystal surface.

On the other hand, the photocatalytic behaviour of the bulk microcrystals follows a pseudo-zero-order kinetic model, where the degradation rate is independent of the RhB concentration and is described by the equation $C/C_0 = -kt + 1$. As shown in Fig. S9b, the linear fit yields a higher correlation coefficient of $R^2 = 0.98$, but with a significantly lower rate constant of $k = 0.0111\ \text{min}^{-1}$. This suggests that the reaction is limited by the intrinsic properties of the microcrystals, such as longer diffusion paths for charge carriers, reduced surface area, and increased probability of electron–hole recombination.

These contrasting kinetic regimes highlight the superior photocatalytic performance of the $Cs_2AgBiBr_6$ nanocrystals, driven by their enhanced surface properties and efficient charge transport characteristics.

To evaluate the photocatalytic stability and recyclability of the $Cs_2AgBiBr_6$ nanocrystals, a three-cycle degradation test was carried out under slightly modified conditions: 100 mg of catalyst were dispersed in 200 mL of RhB solution and exposed to visible light for 40 minutes per cycle. Unlike the kinetic experiments, this test involved only two sampling points per cycle (initial and final concentrations), as our focus was not on reaction kinetics but rather on assessing the material's stability under operational conditions. As shown in Fig. S10, the nanocrystals retained excellent photocatalytic performance, achieving over 99% RhB degradation even in the third cycle, indicating good photocatalytic stability.

Additionally, the photocatalytic properties of the nanocrystals were further analysed by degrading methyl orange (MO). This dye was selected due to its anionic nature, in contrast to the cationic character of RhB. The experiment was performed under the same conditions as for RhB and in triplicate. Fig. S11 shows the degradation of MO along with the corresponding standard deviation. It is evident that the degradation is slower than that of RhB, reaching 80% degradation after 120 min and following a linear trend. In comparison, a previous report showed only 40% degradation of MO after 120 min using 20 mg of bulk-derived $Cs_2AgBiBr_6$ in just 10 mL of MO solution under similar irradiation conditions.[25] This improvement can be attributed to the enhanced surface area and improved charge carrier dynamics of our nanocrystals. These results clearly demonstrate the advantages of nanostructuring in enhancing both the photophysical and surface properties of the catalyst, leading to improved performance under visible light irradiation.

Finally, EPR measurements were performed (Fig. 5a) on a Jeol JES TE-300 X-band spectrometer (1.4 T, TE011 cavity) at room temperature. A suspension of 15 mg of $Cs_2AgBiBr_6$ nanocrystals in 400 μL of ethanol with 2 μL of DMPO was irradiated with a 160 mW Hg lamp ($\lambda = 400$ nm). While low signals were observed in the dark, the characteristic peaks of the DMPO–$^{\bullet}O_2^-$ radical adduct appeared clearly after 5 min of

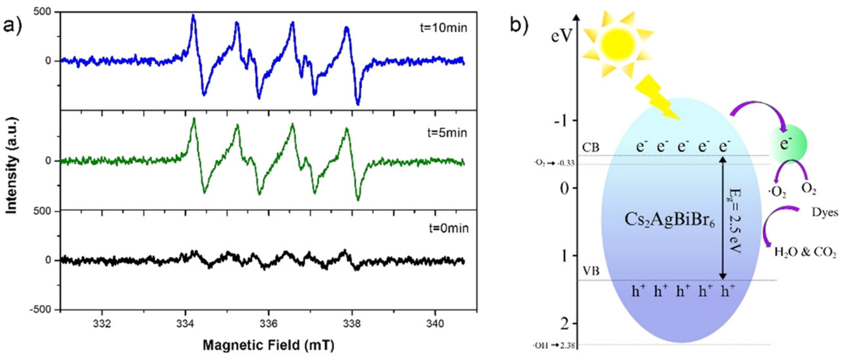

Fig. 5 (a) Electron Spin Resonance (EPR) measurements; (b) proposed pathway for dye degradation, dominated by $^{\bullet}O_2^-$ radicals.

irradiation. The detection of superoxide radicals provides direct experimental confirmation of their central role in the photocatalytic process. Previous studies on $Cs_2AgBiBr_6$ and related double perovskites have consistently reported that dye degradation proceeds through a radical pathway dominated by $^{\bullet}O_2^-$, while h^+ acts as a secondary oxidant and $^{\bullet}OH$ contributes only marginally.[24,25,39] The energetic positions of the electronic bands provide a thermodynamic rationale for this pathway. Reported CB edge values for $Cs_2AgBiBr_6$ range from −0.3 to −1.0 V *vs.* NHE,[24,25,39] which are sufficiently negative to reduce O_2 to $^{\bullet}O_2^-$. Combined with our measured band gap of 2.5 eV, this places the VB between +1.5 and +2.2 V *vs.* NHE, which is less favourable for the generation of $^{\bullet}OH$ through either H_2O or OH^- oxidation. This explains why $^{\bullet}O_2^-$ is the dominant species. Taken together, these findings reinforce that nanostructuring $Cs_2AgBiBr_6$ enhances charge carrier separation and interfacial reactivity, boosting $^{\bullet}O_2^-$ production and thereby accelerating the photocatalytic degradation of organic dyes. The generated superoxide radicals attack the adsorbed dye molecules, initiating aromatic ring cleavage and stepwise oxidation into small intermediates, which are eventually mineralised to CO_2 and H_2O. This mechanistic pathway, widely supported in the literature, is summarised schematically in Fig. 5b, providing a coherent explanation for the high photocatalytic efficiency observed in our nanocrystals.

Conclusions

This work presents a novel, efficient and environmentally friendly ultrasound-assisted method for the synthesis of $Cs_2AgBiBr_6$ nanocrystals at room temperature and in ambient air, demonstrating significant improvements in photocatalytic performance. The resulting nanocrystals exhibit a remarkable enhancement in the degradation of rhodamine B under visible light, achieving nearly complete degradation in just 60 minutes, which is significantly faster compared to bulk microcrystalline $Cs_2AgBiBr_6$. The small particle size (~6 nm) and high surface area of the nanocrystals facilitate efficient charge carrier separation, leading to an accelerated photocatalytic reaction.

Structural characterisation using X-ray diffraction (XRD) and Raman spectroscopy confirms the high purity and stability of the $Cs_2AgBiBr_6$ phase, with no secondary phases being detected. The optical properties of the nanocrystals, characterised by an indirect bandgap of approximately 2.5 eV, further confirm their suitability for visible light-driven photocatalysis.

Moreover, photocatalytic kinetic analysis reveals that the nanocrystals follow a pseudo-first-order reaction model, indicative of efficient surface-driven processes, whereas the bulk powder exhibits a diffusion-limited pseudo-zero-order behaviour. These findings underscore the critical role of nanostructuring in enhancing the photocatalytic performance of $Cs_2AgBiBr_6$, where increased surface area and reduced particle size significantly improve charge transport and minimize electron–hole recombination.

Photocatalytic tests reveal excellent stability and recyclability over multiple cycles, with the nanocrystals maintaining over 99% rhodamine B degradation even after three consecutive uses. The nanocrystals also demonstrate versatility, efficiently degrading methyl orange at a slower rate compared to rhodamine B degradation, highlighting the influence of dye properties on reaction kinetics.

Electron paramagnetic resonance (EPR) measurements confirm the generation of superoxide radicals ($^{\bullet}O_2^-$) under visible-light irradiation, supporting a surface-mediated photocatalytic mechanism where $^{\bullet}O_2^-$ acts as the primary oxidant, while holes (h^+) and hydroxyl radicals ($^{\bullet}OH$) contribute minimally.

The scalability and simplicity of the ultrasound-assisted synthesis method, performed without an inert atmosphere or high-temperature steps, combined with the superior photocatalytic efficiency of the resulting nanocrystals, position this approach as a promising strategy for the development of advanced, eco-friendly materials for sustainable energy and environmental applications.

Conflicts of interest

There are no conflicts to declare.

Data availability

The data supporting this article have been included as part of the SI. The SI contains details on the reagents, synthesis procedures, a schematic of the synthesis process, as well as descriptions of the characterisation techniques and the complementary results. See DOI: https://doi.org/10.1039/d5dt01406a.

Acknowledgements

The authors acknowledge A. Gomez-Cortés for technical support, A. Morales for XRD diffraction patterns, S. Tehuacanero-Cuapa and R. Hernández-Reyes for HRTEM analysis, and C. Zorrilla for Raman spectroscopy. Nora S. Portillo-Vélez (CVU 291032) thanks CONAHCyT for the scholarship "Estancias Posdoctorales 2022(2)". H. A. Lara-García acknowledges the financial support from PAPIIT-UNAM (IA107023 and IN106725), the SECIHTI project CBF-2025-I-2241 and PIIF3. The work of Yesenia A. García-Jomaso was supported by UNAM Posdoctoral Program (POSDOC).

References

1 Y. Dong, Y. Zhao, S. Zhang, Y. Dai, L. Liu, Y. Li and Q. Chen, *J. Mater. Chem. A*, 2018, **6**, 21729–21746.
2 S.-T. Ha, R. Su, J. Xing, Q. Zhang and Q. Xiong, *Chem. Sci.*, 2017, **8**, 2522–2536.
3 P. Acharyya, K. Kundu and K. Biswas, *Nanoscale*, 2020, **12**, 21094–21117.

4 M. H. Miah, M. U. Khandaker, M. J. Hossen, N.-E. Ashrafi, I. Jahan, M. Shahinuzzaman, M. Nur-E-Alam, M. Y. Hanfi, M. H. Ullah and M. A. Islam, *Mater. Adv.*, 2025, **6**, 2718–2752.

5 Z. Wu, H. Tüysüz, F. Besenbacher, Y. Dai and Y. Xiong, *Nanoscale*, 2023, **15**, 5598–5622.

6 G. García-Espejo, D. Rodríguez-Padrón, R. Luque, L. Camacho and G. de Miguel, *Nanoscale*, 2019, **11**, 16650–16657.

7 X. Chen, M. Jia, W. Xu, G. Pan, J. Zhu, Y. Tian, D. Wu, X. Li and Z. Shi, *Adv. Opt. Mater.*, 2023, **11**, 2202153.

8 H. Lei, D. Hardy and F. Gao, *Adv. Funct. Mater.*, 2021, **31**, 2105898.

9 X. Yang, W. Wang, R. Ran, W. Zhou and Z. Shao, *Energy Fuels*, 2020, **34**, 10513–10528.

10 J. Huang, H. Xiang, R. Ran, W. Zhou, W. Wang and Z. Shao, *Renewable Sustainable Energy Rev.*, 2024, **191**, 114187.

11 D. Yang, Y. Guo, Y. Li, B. Hu, B. Yu and Q. Duan, *Org. Chem. Front.*, 2025, **12**, 3887–3895.

12 P. Tian, Y. Ding, F. Zhang, Y. Zhang, J. Wei and J. Chen, *ChemSusChem*, 2025, **18**, e202402106.

13 A. D. Sheikh, H. M. Yadav, K. K. Sharma, J. W. Shim, J. Lee and M. A. Ghanem, *Small*, 2025, **21**, 2501570.

14 V. Chandrabose, M. Bhasuran, R. B. Nair and S. Kurian, *ACS Appl. Energy Mater.*, 2025, **8**, 4574–4585.

15 M. Méndez-Galván, B. Alcántar-Vázquez, G. Diaz, I. A. Ibarra and H. A. Lara-García, *React. Chem. Eng.*, 2021, **6**, 828–838.

16 L. Schade, A. D. Wright, R. D. Johnson, M. Dollmann, B. Wenger, P. K. Nayak, D. Prabhakaran, L. M. Herz, R. Nicholas, H. J. Snaith and P. G. Radaelli, *ACS Energy Lett.*, 2019, **4**, 299–305.

17 R. L. Z. Hoye, L. Eyre, F. Wei, F. Brivio, A. Sadhanala, S. Sun, W. Li, K. H. L. Zhang, J. L. MacManus-Driscoll, P. D. Bristowe, R. H. Friend, A. K. Cheetham and F. Deschler, *Adv. Mater. Interfaces*, 2018, **5**, 1800464.

18 A. H. Slavney, T. Hu, A. M. Lindenberg and H. I. Karunadasa, *J. Am. Chem. Soc.*, 2016, **138**, 2138–2141.

19 L. Zhou, Y. Xu, B. Chen, D. Kuang and C. Su, *Small*, 2018, **14**, 1703762.

20 Z. Liu, H. Yang, J. Wang, Y. Yuan, K. Hills-Kimball, T. Cai, P. Wang, A. Tang and O. Chen, *Nano Lett.*, 2021, **21**, 1620–1627.

21 X. Huang, K. Yin, S. Zhang, T. Wu, Y. Yuan, X. Wang, Y. Jia, Z. Xiao, J. Gu and D. Wang, *Appl. Surf. Sci.*, 2023, **637**, 157877.

22 S. Zhang, Y. Yuan, J. Gu, X. Huang, P. Li, K. Yin, Z. Xiao and D. Wang, *Appl. Surf. Sci.*, 2023, **609**, 155446.

23 W. Xiong, Y. Dong and A. Pan, *Nanoscale*, 2023, **15**, 15619–15625.

24 Q. Fan, S. Wei, J. Ma, W. Zhang and L. Wen, *J. Mater. Chem. A*, 2022, **10**, 14923–14932.

25 Z. Zhang, Y. Liang, H. Huang, X. Liu, Q. Li, L. Chen and D. Xu, *Angew. Chem.*, 2019, **131**, 7341–7345.

26 B. Martinelli, J. A. dos S. Laranjeira, C. L. Ücker, G. M. N. Fabra, J. E. F. S. Rodrigues, R. S. Silva, J. A. Alonso, J. R. Sambrano and M. M. Ferrer, *J. Alloys Compd.*, 2025, **6**, 100064.

27 J. Wu, X. Wang, J. Hu, C. Li, L. Shi, S.-S. Xia, Y. Cai, R. Jia, Z. Chen and L. Li, *J. Environ. Sci.*, 2025, **152**, 577–583.

28 P. Pistor, M. Meyns, M. Guc, H.-C. Wang, M. A. L. Marques, X. Alcobé, A. Cabot and V. Izquierdo-Roca, *Scr. Mater.*, 2020, **184**, 24–29.

29 D. Wu, Y. Tao, Y. Huang, B. Huo, X. Zhao, J. Yang, X. Jiang, Q. Huang, F. Dong and X. Tang, *J. Catal.*, 2021, **397**, 27–35.

30 M. S. Sena, J. Cui, Y. Baghdadi, E. Rattner, M. Daboczi, A. L. Lopes-Moriyama, A. G. dos Santos and S. Eslava, *ACS Appl. Energy Mater.*, 2023, **6**, 10193–10204.

31 Y. Zhang, T. Shah, F. L. Deepak and B. A. Korgel, *Chem. Adv. Mater.*, 2019, **31**, 7962–7969.

32 J. Liu, A. A. Vedernikova, Q. Xue, H. Gao, X. Xie, J. Xie, E. V. Ushakova, H. Huang and X. Zhang, *Adv. Sci.*, 2025, **12**, 2416046.

33 Y. Bekenstein, J. C. Dahl, J. Huang, W. T. Osowiecki, J. K. Swabeck, E. M. Chan, P. Yang and A. P. Alivisatos, *Nano Lett.*, 2018, **18**, 3502–3508.

34 A. Mondal, M. Ahuja, P. Johari and S. Bhattacharyya, *Chem. Commun.*, 2024, **60**, 3693–3696.

35 J. Wu, X. Wang, J. Hu, C. Li, L. Shi, S. S. Xia, Y. Cai, R. Jia, Z. Chen and L. Li, *J. Environ. Sci.*, 2025, **152**, 577–583.

36 S. J. Zelewski, J. M. Urban, A. Surrente, D. K. Maude, A. Kuc, L. Schade, R. D. Johnson, M. Dollmann, P. K. Nayak, H. J. Snaith, P. Radaelli, R. Kudrawiec, R. J. Nicholas, P. Plochocka and M. Baranowski, *J. Mater. Chem. C*, 2019, **7**, 8350–8356.

37 A. D. Wright, L. R. V. Buizza, K. J. Savill, G. Longo, H. J. Snaith, M. B. Johnston and L. M. Herz, *J. Phys. Chem. Lett.*, 2021, **12**, 3352–3360.

38 G. Longo, S. Mahesh, L. R. V. Buizza, A. D. Wright, A. J. Ramadan, M. Abdi-Jalebi, P. K. Nayak, L. M. Herz and H. J. Snaith, *ACS Energy Lett.*, 2020, **5**, 2200–2207.

39 M. Yang, R. Wang, J. Yang, Y. Zhao, H. Song and H. Wang, *Surf. Interfaces*, 2025, **56**, 105687.